LETTER

doi:10.1038/nature13963

Evolution and forcing mechanisms of El Niño over the past 21,000 years

Zhengyu Liu[1,2], Zhengyao Lu[2], Xinyu Wen[2], B. L. Otto-Bliesner[3], A. Timmermann[4] & K. M. Cobb[5]

The El Niño Southern Oscillation (ENSO) is Earth's dominant source of interannual climate variability, but its response to global warming remains highly uncertain[1]. To improve our understanding of ENSO's sensitivity to external climate forcing, it is paramount to determine its past behaviour by using palaeoclimate data and model simulations. Palaeoclimate records show that ENSO has varied considerably since the Last Glacial Maximum (21,000 years ago)[2–9], and some data sets suggest a gradual intensification of ENSO over the past ~6,000 years[2,5,7,8]. Previous attempts to simulate the transient evolution of ENSO have relied on simplified models[10] or snapshot[11–13] experiments. Here we analyse a series of transient Coupled General Circulation Model simulations forced by changes in greenhouse gasses, orbital forcing, the meltwater discharge and the ice-sheet history throughout the past 21,000 years. Consistent with most palaeo-ENSO reconstructions, our model simulates an orbitally induced strengthening of ENSO during the Holocene epoch, which is caused by increasing positive ocean–atmosphere feedbacks. During the early deglaciation, ENSO characteristics change drastically in response to meltwater discharges and the resulting changes in the Atlantic Meridional Overturning Circulation and equatorial annual cycle. Increasing deglacial atmospheric CO_2 concentrations tend to weaken ENSO, whereas retreating glacial ice sheets intensify ENSO. The complex evolution of forcings and ENSO feedbacks and the uncertainties in the reconstruction further highlight the challenge and opportunity for constraining future ENSO responses.

To understand ENSO's evolution during the past 21 kyr, we analyse the baseline transient simulation (TRACE) conducted with the Community Climate System model version 3 (CCSM3). This simulation uses the complete set of realistic climate forcings: orbital, greenhouse gases, continental ice sheets and meltwater discharge (Fig. 1a, d and Methods). TRACE has been shown to replicate many key features of the global climate evolution[14,15]. Over the tropical Pacific, the annual mean sea surface temperature (SST) closely tracks atmospheric CO_2 (Fig. 1d); the cross-equatorial eastern Pacific meridional SST gradient largely tracks the meltwater forcing and the resulting change in the Atlantic Meridional Overturning Circulation (AMOC), a situation consistent with proxy evidence[15] (Fig. 1b, c). ENSO amplitude changes in a complex pattern, as seen in the interannual SST variability over the central-eastern Pacific (Fig. 1e, Extended Data Fig. 1 and Methods). In 100-year windows, ENSO amplitude varies considerably on a multitude of timescales (Extended Data Fig. 2a), in a similar manner to those in other multi-millennial simulations[16] and in palaeo-ENSO reconstructions from lake sediments[2,7,17] (Fig. 1e) and fossil corals[6] from ENSO-teleconnected regions. The unforced variance changes in ENSO may originate from the nonlinear dynamics of ENSO[10] and/or stochastic climate forcings[18,19].

Beyond the background irregularity of ENSO amplitude, however, there are externally forced changes (Fig. 1e and Extended Data Fig. 2a), such as a reduction in ENSO amplitude just after the Last Glacial Maximum (LGM) before levelling off during the Heinrich Stadial 1 (HS1, ~17 kyr ago), a rapid weakening related to the AMOC resumption at the onset of the Bølling–Allerod (BA, ~14.5 kyr ago) and an increase during the Younger Dryas (YD, ~12.9–11.7 kyr ago). During the Holocene,

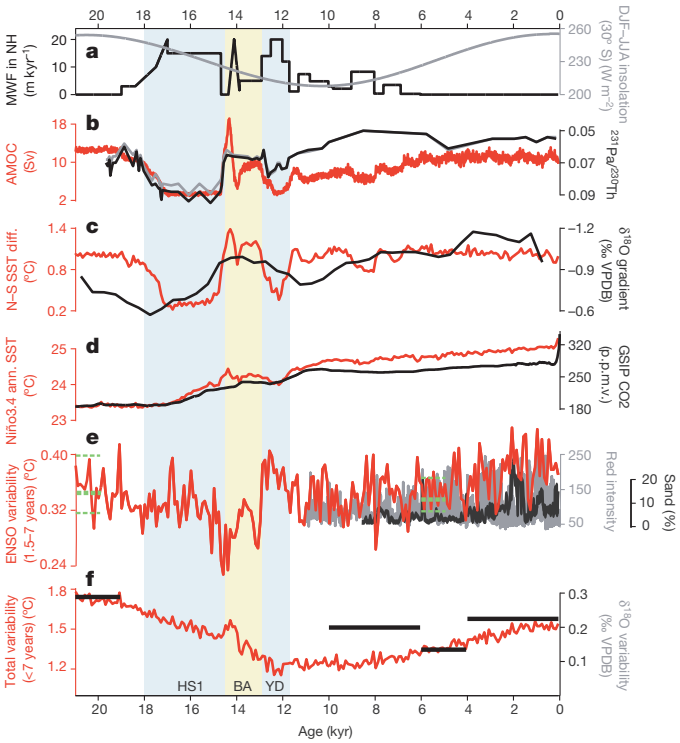

Figure 1 | TRACE simulation and observation. **a**, Grey, amplitude of annual cycle of insolation (December, January and February minus June, July and August (DJF–JJA)) at 30° S (Methods); black, meltwater flux into the North Atlantic (in equivalent sea level change in metres per 1,000 years). **b**, Red, AMOC transport (in sverdrups (Sv); 1 Sv = 10^6 m^3 s^{-1}); black and grey, $^{231}Pa/^{230}Th$ ratio in Bermuda (Methods). **c**, Red, eastern Pacific north–south difference in annual SST (5–15° N minus 5°–15° S, 140–100° W); black, reconstruction[5]. VPDB, Vienna Pee Dee Belemnite. **d**, Red, Niño3.4 (170–120° W, 5° S–5° N) annual SST; black, Niño3.4 CO_2 reconstruction (Methods). **e**, Red, ENSO amplitude (standard deviation of Niño3.4 interannual (1.5–7 years) SST variability) in 100-year windows; black, lake sediment records in the eastern Pacific (El Juno)[7]; grey, lake sediment records on the South American coast (Lake Laguna Pallcacocha)[2]. The green bars at 6 and 21 kyr ago represent the median (solid) and 75th and 25th centiles (dashes) of ENSO amplitude changes in the mid-Holocene and LGM experiments in the PMIP2/PMIP3 ensemble[20] (rescaled using TRACE ENSO in the late Holocene 2–0 kyr ago). **f**, Amplitude (standard deviation) of Niño3 (150–90° W, 5° S–5° N) SST total variability (less than 7 years) in 100-year windows. The black bars show the reconstruction of total SST variance derived from sediment cores in the eastern equatorial Pacific[5].

[1]Department of Atmospheric and Oceanic Sciences and Nelson Center for Climatic Research, University of Wisconsin-Madison, Madison, Wisconsin 53706, USA. [2]Laboratory of Climate, Ocean and Atmosphere Studies, School of Physics, Peking University, Beijing, 100871, China. [3]Climate and Global Dynamics Division, National Center for Atmospheric Research, Boulder, Colorado 80307-3000, USA. [4]International Pacific Research Center and Department of Oceanography, School of Ocean and Earth Science and Technology, University of Hawaii at Manoa, Honolulu, Hawaii 96822, USA. [5]School of Earth and Atmospheric Sciences, Georgia Institute of Technology, Atlanta, Georgia 30332, USA.

ENSO gradually intensified by ~15%. The simulated ENSO evolution is qualitatively similar to that in other models at 6 and 21 kyr ago, falling within the spread of the Palaeoclimate Modelling Intercomparison Project 2 (PMIP2)/PMIP3 ensemble[20] (Fig. 1e).

The simulated ENSO intensification over the Holocene is qualitatively consistent with several key ENSO-sensitive proxy records (Fig. 1e), such as the increase in precipitation variability along the South American coast throughout the Holocene[2,4,7] (Extended Data Figs 3a, b, 4c, d and 5c and Methods), and the increase in ENSO variance in the western Pacific fossil corals from the mid to late Holocene[3]. An intensification of ENSO during the Holocene is also inferred from the ensemble spread of SST from foraminifera in the eastern Pacific[5], although this ensemble spread probably more reflects the total SST variability, which is dominated by the annual cycle rather than ENSO there (Fig. 1f and Extended Data Fig. 2b). Nevertheless, the most recent reconstructions of ENSO's evolution over the Holocene suggest that ENSO variance reached a minimum around the mid Holocene[5,6,21] (Fig. 1f and Extended Data Fig. 6b), with a decrease of ~30–50% relative to the late Holocene. Such a trajectory is not inconsistent with previously published palaeo-ENSO data sets, given their small sample size relative to the high level of intrinsic variability in ENSO amplitudes (Extended Data Figs 2b, c and 6 and Methods).

The simulated trend in Niño3.4 variance over the Holocene amounts to +15%, which is consistent with most mid-Holocene PMIP2/PMIP3 experiments, which show increases of 10–15% in ENSO variance from 6 kyr ago to pre-industrial conditions[20] (Fig. 1e). If the response of ENSO to precessional forcing was indeed relatively modest as in current models, the available palaeo-ENSO data sets are as yet too sparse to detect such a subtle shift in the Holocene, given the high level of background variability[6] (Methods). If, in contrast, ENSO did intensify by 50% and did reach the minimum in the mid-Holocene, the inconsistent simulations in current models would imply model deficiencies. The ultimate resolution of the detailed evolution characteristics of ENSO variance in the Holocene will require much more high-resolution palaeoclimate data from ENSO centres of action.

The comparison with observations before the Holocene poses an even deeper challenge because proxy records of ENSO are rare and less consistent. The few coral records scattered across the last glacial period suggest an active ENSO presence[3,22], but the coral records are too short and sparse to provide a robust estimation of ENSO intensity changes[6] (Methods). Other records seem to show conflicting results. The lithic flux rate associated with flood events in a sediment record off Peru has been used to argue for the change in ENSO-related flooding event, which is weaker at the LGM than the late Holocene[8], as also implied by a varve record in east Africa[17]. The lithic flux data further imply that ENSO intensified rapidly from 17 to 13 kyr ago before gradually peaking at 8 kyr ago[8]. However, the variability of eastern equatorial Pacific subsurface temperatures reconstructed from subsurface dwelling planktonic foraminifera suggests a modestly stronger ENSO at the LGM, which then intensifies to peak at 15 kyr ago and then weakens towards the minimum at 8 kyr ago[9]. The PMIP2/PMIP3 experiments also show a wide spread of ENSO's response at the LGM with no statistically significant change in the ensemble mean ENSO at the LGM relative to the late Holocene[20]. The ENSO amplitude in TRACE is reduced by ~0.2 °C at the LGM relative to the late Holocene, well within the spread of the PMIP2/PMIP3 experiments (Fig. 1e). The inconsistent ENSO responses during the deglaciation, among data and among models, could be caused by various factors. The use of palaeoclimate records in remote regions as proxies for ENSO variance should be treated with caution, especially for those sites outside the region of strong ENSO impact (Extended Data Fig. 4a, b and Methods), where the trend of precipitation variance is dominated by the local response to deglacial climate forcings (Extended Data Fig. 5a, b), rather than by ENSO effects. In addition, the relation between the proxy variance and ENSO variance could change over time, as seen in the less consistent variance between precipitation and ENSO during the deglaciation than during the Holocene in the model (Extended Data Figs 3c–e and 5a, b and Methods). The intrinsic irregularity of ENSO[16] itself also calls into question the use of snapshots of ENSO amplitude, both in palaeoclimate data and in climate models, to represent the continuous evolution.

To determine the physical mechanisms that cause millennial to orbital-scale changes in ENSO strength in TRACE, we quantify the time evolution of ocean–atmosphere feedbacks in the eastern Pacific by using the Bjerknes (BJ) index, which consists of three positive feedbacks (upwelling feedback, zonal advection feedback and thermocline feedback) and two negative feedbacks (heat flux feedback and mean advection feedback)[23] (Methods). In the Holocene, both the BJ index (Fig. 2d) and ENSO amplitude (Fig. 2b) increase in unison (positive correlation of 0.5; $P = 0.004$, 10–0 kyr ago), suggesting a contribution of positive ocean–atmosphere feedback to ENSO intensification. The BJ index increases primarily as a result of the upwelling feedback (Extended Data Fig. 7b). All the positive feedbacks increase throughout the Holocene by means of increased wind sensitivity to SST (Extended Data Fig. 8a), probably related to the warming trend in annual mean climatology (Fig. 1d) that favours active moisture convection and in turn an enhanced atmospheric response to SST anomalies[11]. The tropical warming is forced mainly by the increased annual mean insolation in response to the decreasing obliquity[24] and increasing CO_2. The upwelling feedback is further amplified by the intensified stratification of the upper ocean (Extended Data Fig. 8f), which is generated by the increased austral winter cooling over the subtropical South Pacific (Fig. 2a) and the subsequent equatorward ventilation[12] (Extended Data Fig. 9 and Methods). Thus, the intensifying ENSO in the Holocene is caused mainly by enhanced positive ocean–atmosphere feedbacks, especially the upwelling feedback, in response to precessional forcing.

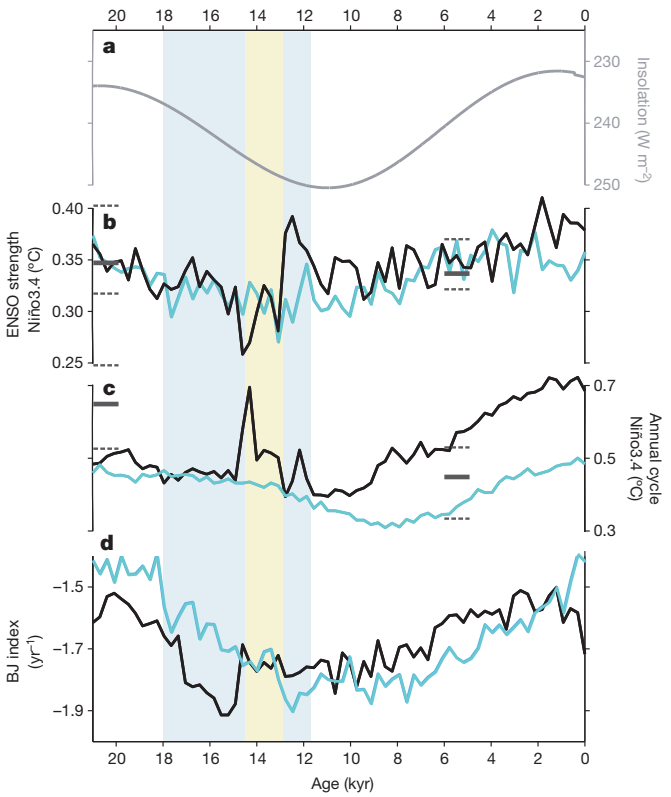

Figure 2 | ENSO, BJ index and annual cycle. **a**, Austral winter (JJA) insolation at 30° S. **b**–**d**, The amplitude of ENSO (**b**), the annual cycle of Niño3.4 SST (**c**) and the BJ index (**d**) in the eastern equatorial Pacific (180–80° W, 5° S–5° N). All are calculated in 300-year windows with black for TRACE and cyan for ORB. In **b** and **c** the grey bars at 6 and 21 kyr ago represent the median (solid) and 75th and 25th centiles (dashes) of the amplitudes of ENSO and annual cycle in the mid-Holocene and LGM experiments in the PMIP2/PMIP3 ensemble[20] (rescaled using TRACE in the late Holocene 2–0 kyr ago).

The dominant role of precessional forcing on ENSO evolution is further confirmed by a sensitivity experiment forced by only orbital forcing (ORB; Methods). The ORB experiment almost reproduces the slow trends of ENSO (Fig. 2b), the annual cycle (Fig. 2c) and the BJ index (Fig. 2d) in TRACE throughout the 21 kyr, except for the millennial-scale events associated with changes in the AMOC during the early deglaciation (Fig. 2b, c). Therefore, the overall evolution of ENSO, with an initial weakening towards the early Holocene and a subsequent strengthening towards the late Holocene, is determined largely by the strength of the ocean–atmosphere feedback (Fig. 2d) and its response to precessional forcing (Fig. 2a). The annual cycle of eastern Pacific SST also weakens towards the early Holocene and recovers towards the late Holocene. This change in annual cycle is caused by the annual cycle of insolation in the subtropical South Pacific (Fig. 1a), which forces a local annual cycle that propagates equatorwards as a result of air–sea interactions[25]. The minimum amplitude of annual cycle in the early to mid Holocene is also qualitatively consistent with PMIP2/PMIP3 experiments for 6 kyr ago and the LGM (Fig. 2c).

In contrast to ENSO's response to precessional forcing, the millennial variability of ENSO's intensity during the early deglaciation is caused by the changes in the annual cycle amplitude triggered by deglacial meltwater fluxes and the resulting AMOC responses. Indeed, the millennial swings of ENSO amplitude often change out of phase with the BJ index, notably around HS1 and YD (Fig. 2b, d and Extended Data Fig. 7a), and therefore cannot be explained by changing ocean–atmosphere instability as with orbital forcing. There is thus no significant correlation between ENSO intensity and the BJ index (0.09; $P = 0.58$, 21–10 kyr ago). Instead, the millennial ENSO variance (Fig. 2b) tends to vary out of phase with the amplitude of the annual cycle (Fig. 2c), with a highly significant negative correlation of −0.49 ($P = 0.002$, 21–10 kyr ago). The close interaction between ENSO and the annual cycle is also consistent with the strong phase-locking of ENSO during early deglaciation (Extended Data Fig. 10). A meltwater pulse in the North Atlantic (Fig. 1a) decreases the AMOC (Fig. 1b), shifts the Intertropical Convergence Zone (ITCZ) southwards and creates an equatorially more symmetric annual mean climate in the eastern equatorial Pacific, corresponding to a weaker north–south difference in SST (Fig. 1c) and a weaker equatorial annual cycle (Fig. 2c)[26]; the weaker annual cycle then amplifies ENSO through the nonlinear mechanism of frequency entrainment[26,27]. The anti-correlation between annual cycle strength and ENSO variance has also been observed for other external forcings in many Coupled General Circulation Models (CGCMs)[28]. The role of the meltwater forcing is confirmed explicitly in a transient sensitivity experiment forced by the deglacial meltwater flux alone (MWF). In the MWF, ENSO's amplitude (Fig. 3a, blue) varies largely out of phase with that of the annual cycle (Fig. 3b, blue) at millennial timescales, in a similar manner to TRACE.

The dominant roles of precessional and meltwater forcings for the deglacial evolution of ENSO raises the question: what is the role of CO_2 forcing on ENSO? To address this question, we analyse an additional sensitivity experiment forced by the greenhouse gases alone (CO2). In CO2, ENSO weakens gradually from 17 to 12 kyr ago (Fig. 3a), following the rising CO_2 (Fig. 1c). The ENSO weakening in CCSM3 can be caused by a more diffusive equatorial thermocline forced by the CO_2 warming[29], and a more asymmetric tropical warming around the Equator and in turn a stronger annual cycle (Fig. 3b) through frequency entrainment[30]. This CO_2-induced ENSO weakening can be detected in TRACE as the gradual reduction of ENSO from 17 kyr ago towards the BA (~14.5 kyr ago). However, the weakening leaves little net signal after the BA (Fig. 3a), because of the offset by the ENSO amplification associated with the retreat of the ice sheet at ~14 kyr ago. As shown in another sensitivity experiment forced by the ice sheet alone (ICE), ENSO is amplified abruptly at 14 kyr ago by a large retreat of the ice sheet over North America (Fig. 3a). The retreat of the ice sheet changes the atmospheric jet and, in turn, the tropical Pacific climatology through teleconnections, which lead to a weaker equatorial annual cycle (Fig. 3b and Methods) and eventually a strengthening ENSO again through frequency entrainment[27]. The

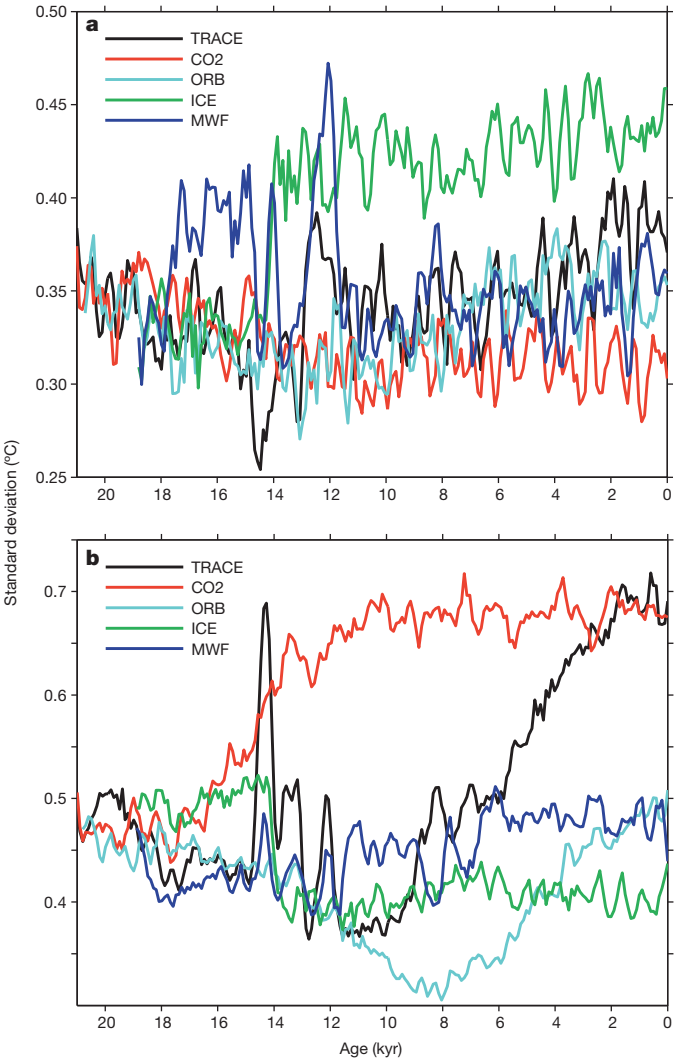

Figure 3 | ENSO in single forcing experiments. **a**, Amplitude of ENSO. **b**, Amplitude of the annual cycle. The amplitude is calculated as the standard deviation of Niño3.4 SST in the frequency band of 1.5–7 years for ENSO, and for the composite seasonal cycle for the annual cycle, both in 300-year windows. The natural variability of the ENSO amplitude can be estimated approximately from the Holocene part of CO2, MWF and ICE as a standard deviation of ~0.2 °C.

opposite effects of CO_2 and the ice sheet on ENSO amplitude offer an explanation of why, unlike the robust ENSO response in the Holocene, the response of ENSO amplitude at the LGM differs between models[20]. At the LGM, because the precessional forcing is similar to that in the late Holocene, ENSO is affected by two large forcings with opposite effects: the lower CO_2 and the presence of large ice sheets.

Overall, the ENSO evolution reconstructed from available proxy records seems to be qualitatively consistent with the simulated ENSO strengthening during the Holocene. However, the proxy data must be improved significantly to help constrain climate models better for the simulation of ENSO evolution in the past and, eventually, for the model projections of the future.

Online Content Methods, along with any additional Extended Data display items and Source Data, are available in the online version of the paper; references unique to these sections appear only in the online paper.

Received 30 June; accepted 7 October 2014.

1. Collins, M. *et al.* The impact of global warming on the tropical Pacific ocean and El Nino. *Nature Geosci.* **3,** 391–397 (2010).
2. Moy, C. *et al.* Variability of El Niño/Southern Oscillation activity at millennial timescales during the Holocene epoch. *Nature* **420,** 162–166 (2002).

3. Tudhope, A. *et al.* Variability in the El Niño–Southern Oscillation through a glacial–interglacial cycle. *Science* **291,** 1511–1517 (2001).
4. Riedinger, M. *et al.* A ~6100 ^{14}C yr record of El Niño activity from the Galapagos islands. *J. Paleolimnol.* **27,** 1–7 (2002).
5. Koutavas, A. & Joanides, S. El Niño–Southern Oscillation extrema in the Holocene and Last Glacial Maximum. *Paleoceanography* **27,** PA4208, http://dx.doi.org/10.1029/2012PA002378 (2012).
6. Cobb, K. *et al.* Highly variable El Niño–Southern Oscillation throughout the Holocene. *Science* **339,** 67–70 (2013).
7. Conroy, J. *et al.* Holocene changes in eastern tropical Pacific climate inferred from a Galapagos lake sediment record. *Quat. Sci. Rev.* **27,** 1166–1180 (2008).
8. Rein, B. *et al.* El Niño variability off Peru during the last 20,000 years. *Paleoceanography* **20,** PA4003, http://dx.doi.org/10.1029/2004PA001099 (2005).
9. Sadekov, A. *et al.* Paleoclimate reconstructions reveal a strong link between El Niño-Southern Oscillation and tropical Pacific mean state. *Nature Commun.* **4,** 2692, http://dx.doi.org/10.1038/ncomms3692 (2013).
10. Clement, A., Seager, R. & Cane, M. Suppression of El Niño during the Mid-Holocene by changes in the Earth's orbit. *Paleoceanography* **15,** 731–737 (2000).
11. Roberts, W. *An Investigation into the Causes for the Reduction in the Variability of the El Niño-Southern Oscillation in the Early Holocene in a Global Climate Model.* PhD thesis, Univ. Washington (2007).
12. Liu, Z., Kutzbach, J. & Wu, L. Modeling climatic shift of El Niño variability in the Holocene. *Geophys. Res. Lett.* **27,** 2265–2268 (2000).
13. Otto-Bliesner, B. *et al.* Modeling El Niño and its tropical teleconnections during the glacial–interglacial cycle. *Geophys. Res. Lett.* **30,** 10.1029/2003GL08553 (2003).
14. Liu, Z. *et al.* Transient simulation of last deglaciation with a new mechanism for Bølling–Allerød warming. *Science* **325,** 310–314 (2009).
15. Shakun, J. *et al.* Global warming preceded by increasing CO_2 during the last deglaciation. *Nature* **484,** 49–54 (2012).
16. Wittenberg, A. Are historical records sufficient to constrain ENSO simulations. *Geophys. Res. Lett.* **36,** L12702 (2009).
17. Wolff, C. *et al.* Reduced interannual rainfall variability in East Africa during the Last Ice Age. *Science* **333,** 743–747 (2011).
18. Penland, C. & Sardeshmukh, P. The optimal growth of tropical sea surface temperature anomalies. *J. Clim.* **8,** 1999–2024 (1995).
19. Chiang, J., Fang, Y. & Chang, P. Pacific climate change and ENSO activity in the mid-Holocene. *J. Clim.* **22,** 923–939 (2009).
20. Masson-Delmotte, V. *et al.* In *Climate Change 2013: The Physical Science Basis. Contribution of Working Group I to the Fifth Assessment Report of the Intergovernmental Panel on Climate Change* (eds Stocker, T. F. *et al.*) 383–464 (Cambridge Univ. Press, 2013).
21. Carre, M. *et al.* Holocene history of ENSO variance and asymmetry in the eastern tropical Pacific. *Science* **345,** 1045–1048 (2014).
22. Felis, T. *et al.* Pronounced interannual variability in tropical South Pacific temperatures during Heinrich Stadial 1. *Nature Commun.* **3,** 965, http://dx.doi.org/10.1038/ncomms1973 (2012).
23. Kim, S. & Jin, F. An ENSO stability analysis. Part I: results from a hybrid coupled model. *Clim. Dyn.* **36,** 1593–1607 (2011).
24. Liu, Z., Brady, E. & Lynch-Steiglitz, J. Global ocean response to orbital forcing in the Holocene. *Paleoceanography* **18,** 1041 (2003).
25. Liu, Z. & Xie, S. Equatorward propagation of coupled air–sea disturbances with application to the annual cycle of the eastern tropical Pacific. *J. Atmos. Sci.* **51,** 3807–3822 (1994).
26. Timmermann, A. *et al.* The influence of a weakening of the Atlantic Meridional Overturning Circulation on ENSO. *J. Clim.* **20,** 4899–4919 (2007).
27. Liu, Z. A simple model study of the forced response of ENSO to an external periodic forcing. *J. Clim.* **15,** 1088–1098 (2002).
28. Timmermann, A. *et al.* The effect of orbital forcing on the mean climate and variability of the tropical Pacific. *J. Clim.* **20,** 4147–4159 (2007).
29. Meehl, G., Teng, H. & Branstator, G. Future changes of El Niño in two global climate models. *Clim. Dyn.* **26,** 549–566 (2006).
30. Timmermann, A., Jin, F. & Collins, M. Intensification of the annual cycle in the tropical Pacific due to greenhouse warming. *Geophys. Res. Lett.* **31,** L12208 (2004).

Acknowledgements This work is supported by the US National Science Foundation (NSF)/P2C2 Program, Chinese NSFC41130105, the US Department of Energy/Office of Science (BER), Chinese MOST2012CB955200, NSF1049219 and 1204011. The computation is carried out at Oak Ridge National Laboratory of the Department of Energy and the National Center for Atmospheric Research supercomputing facility.

Author Contributions Z. Liu conceived the study and wrote the paper. Z. Lu and XW performed the analysis. Z. Liu and B.O.B. contributed to the simulations. A.T. and K.C. contributed to the interpretation. All authors discussed the results and provided inputs to the paper.

Author Information Reprints and permissions information is available at www.nature.com/reprints. The authors declare no competing financial interests. Readers are welcome to comment on the online version of the paper. Correspondence and requests for materials should be addressed to Z. Liu (zliu3@wisc.edu).

METHODS

Model and simulations. The model is the Community Climate System Model version 3 (CCSM3)[31] maintained at the National Center for Atmospheric Research (NCAR), with the resolution of T31×'3 and include a dynamic vegetation component and fixed annual cycle of aerosol forcing. As a continuation of the DGL-A simulation of ref. 14, the TRACE experiment is initialized from an equilibrium simulation forced by the LGM forcing (22 kyr ago), and is then forced by the complete set of realistic transient climate forcing, orbital insolation[32] (Fig. 1a), atmospheric greenhouse gases[33] (Fig. 1d) and meltwater discharge (Fig. 1a); the continental ice sheet is modified according to ICE-5G[34], once per 1,000 years for 19–17 kyr ago, and once per 500 years after 17 kyr ago. The coastlines and bathymetry are modified at 13.1 kyr ago with the removal of the Fennoscandian Ice Sheet from the Barents Sea, at 12.9 kyr ago with the opening of the Bering Strait, at 7.6 kyr ago with the opening of Hudson Bay, and finally at 6.2 kyr ago with the opening of the Indonesian Throughflow. Meltwater fluxes largely follow the record of sea level rise and geological indicators of ice sheet retreat and meltwater discharge. The meltwater forcing during mwp-1A consists of contributions from the Antarctic (15 m of equivalent sea-level volume) and Laurentide (5 m of equivalent sea-level volume) Ice Sheets. More details of the TRACE simulation can be found in ref. 35. TRACE reproduces many key features of the response of the climatology in the last 21 kyr as in the reconstruction[14,15], such as the AMOC intensity (Fig. 1b, with black and grey lines being two proxies from ref. 36), cross-Equator SST contrast (Fig. 1c), tropical Pacific SST (Fig. 1d).

Four single forcing experiments are integrated in the same way as TRACE, but each is forced by a single transient forcing only with other forcings fixed at conditions at the start of each simulation[37]. The ORB and CO2 runs are initialized from the TRACE state at 22 kyr ago; ORB is forced by only the transient orbital forcing, and GHG is forced by only the transient greenhouse gas concentrations after 22 kyr ago. The MWF and ICE are initialized at the TRACE state of 19 kyr ago; the MWF is forced by only the transient Northern Hemisphere meltwater fluxes, and ICE is forced by the changing continental ice sheet after 19 kyr ago.

Model ENSO. ENSO simulated by the model for the present day shows many realistic features, although the ENSO period tends to be biased towards quasi-biannual, as opposed to a broader 2–7-year peak in the observation[38]. The ENSO mode resembles the SST mode[29] and propagates westwards as in many CGCMs. In the past 21 kyr, the preferred period of model ENSO remains at quasi-biannual, with the power spectrum changing only modestly with time (Extended Data Fig. 1).

The use of remote precipitation variability to infer the change in ENSO. ENSO's amplitude is defined normally in terms of the interannual SST variance in the central-eastern equatorial Pacific region, typically the Niño3.4 (170°–120° W, 5° S–5° N) or Niño3 (150–90° W, 5° S–5° N) region. A direct measurement of ENSO's amplitude can therefore, in principle, be made only using sufficient number of high-resolution proxies of SST variability, such as fossil corals, in this region[6]. However, because of the insufficient number of direct ENSO proxies, the change in ENSO's amplitude has been often inferred indirectly from other proxies, notably the interannual variance of certain precipitation-sensitive proxies such as sediment fluxes[2,4,7,8] and varve thickness[17,39], in regions that are affected by ENSO teleconnection. This indirect inference may be valid under two conditions. (For simplicity, here, we ignore the issue related to the temporal resolution of the proxy.) First, ENSO teleconnections remain stationary throughout time. Second, the proxy site is located in a region under strong ENSO impact; that is, the precipitation variability is highly correlated with ENSO such that most of its interannual variance is indeed caused by ENSO. Outside the region of strong ENSO impact, a significant part of the interannual variance in precipitation is contributed by local variability independently of ENSO[40]. Nevertheless, the amplitude of precipitation variability can still be correlated with that of ENSO if the local response of interannual precipitation variability to a changing climate forcing, such as the orbital forcing, is similar to that of ENSO, rather than by teleconnection.

CCSM3 reproduces the ENSO teleconnections reasonably well. A comparison of the correlation between the monthly time series of ENSO (Niño3.4 SST) and interannual (1.5–7-yr) variability of precipitation for the present day in TRACE (Extended Data Fig. 4c, 1–0 kyr ago) and the observation (Extended Data Fig. 4d; HadISST and CPC Merged Analysis of Precipitation of 1981–2005) across the globe shows that the model captures the major features of the observed teleconnection, notably the positive correlation extending from the central equatorial Pacific to the South American coast and into the mid-latitude Northern Hemisphere, and the negative correlation surrounding the central-eastern equatorial Pacific, although the magnitude of correlation is somewhat underestimated in the model. In addition, a comparison of the ENSO teleconnection at different periods in TRACE, for example at the LGM (21–20 kyr ago; Extended Data Fig. 4a), early deglaciation (16–15 kyr ago; Extended Data Fig. 4b) and the present (1–0 kyr ago; Extended Data Fig. 4c), shows that the overall features of ENSO teleconnection remain largely unchanged.

In spite of statistically significant ENSO teleconnections globally, the region of strong ENSO impact is confined mainly to the core region of ENSO impact, from the central equatorial Pacific to the South American coast. This core region can be seen as the region with the correlation magnitude above 0.5 in the model (Extended Data Fig. 4a–c). The validity of precipitation variability as a proxy for ENSO amplitude changes in the core region is confirmed by calculation of the interdecadal amplitude correlation between precipitation variability and ENSO. The amplitude is calculated first in a 40-year window from the monthly time series filtered to the band of 1.5–7 years. The local response to slow external forcings, such as orbital and meltwater fluxes, is then filtered by subtracting its 200-year running mean. The high-pass interdecadal amplitude correlation (Extended Data Fig. 4e–h) between the precipitation variance and ENSO variance in the core region of ENSO impact, mainly in the equatorial Pacific to the South American coast, is positive, similar to a previous study[26], and highly correlated (more than 0.6) in the central equatorial Pacific of Niño4 and Niño3.4 regions. This suggests that precipitation proxy records in the core region of ENSO impact can indeed be used to infer the change in ENSO amplitude reasonably well. In the very eastern equatorial Pacific and South American coast, such as the Galapagos islands and Ecuador, precipitation variability is also reasonable for inferring ENSO changes, as seen in Extended Data Fig. 3a, b for the Holocene. Nevertheless, in these regions, the teleconnection correlation is not as large as in the central Pacific region (Extended Data Fig. 4a–d) and the interdecadal amplitude correlation is also weak, usually smaller than 0.4 (Extended Data Fig. 4e–h). Some failures of using precipitation variability to infer the correct trend of ENSO amplitude, for example during the early deglaciation in the Galapagos islands, are therefore possible (Extended Data Fig. 3a).

Outside the core region of ENSO impact, the interdecadal amplitude correlation is usually small (Extended Data Fig. 4e–h) and therefore precipitation variability can usually not be used to infer ENSO changes. However, the slow evolution of precipitation variance can still be correlated with that of ENSO. Extended Data Fig. 5a–c shows the correlation of the low-pass (200-year running mean) amplitude between precipitation variability and ENSO for different periods. The most striking feature is the high positive correlation in the central equatorial Pacific and the South American coast, across all the periods, as in the interdecadal amplitude correlation (Extended Data Fig. 4e–h). This is consistent with the implication of strong ENSO impact in this core region, as discussed in Extended Data Fig. 4.

Further issues on model–data comparison of ENSO changes in the Holocene. Our model–data comparison of ENSO amplitude in the Holocene has focused on the qualitative aspects (Fig. 1e). A quantitative model–data comparison would be much more challenging, because of the data interpretation and sample size as well as model deficiencies[41]. Overall, however, as in other models[20], our model underestimates the ENSO change in the Holocene, about 15%, against some reconstruction of SSTs of 50% or higher[3,21]. However, the small sample size[6,21] may not give a robust estimation of the ENSO amplitude trend[6]. Lake sediments[2,4] also show some large changes, but their interpretations remain elusive, especially for a quantitative comparison. ENSO amplitude is sensitive to the different measures such as the number of strongest events and the frequency of occurrence[41]. Thus, detailed quantitative model–data comparisons should be approached cautiously.

To illustrate the potential uncertainty related to the inherent irregularity of ENSO amplitude[16], we use the Monte Carlo method to test the trend of ENSO amplitude in the Holocene derived in the model as in the coral records of ref. 6. A model 'fossil coral' record is simulated by a 30-year section of the monthly Niño3.4 SST that is randomly selected between 7 and 0 kyr ago. The ENSO amplitude is calculated as the standard deviation of the monthly SST in the frequency band of 1.5–7 years. The linear trend is then derived using a linear regression of the ENSO amplitudes of a set of 50 corals that are randomly selected between 7 and 0 kyr ago. The probability density function (PDF) of the linear trend is then derived from an ensemble of 10,000 sets of 50-member corals (Extended Data Fig. 6a, the red TRACE pdf profile). The null-hypothesis PDF is derived from an ensemble of 10,000 sets of 50-member pseudo-corals from a SST time series that is derived from the original Niño3.4 SST time series between 7 and 0 kyr ago after a random scrambling in time such that any linear trend is destroyed (Extended Data Fig. 6a, the red Null pdf profiles). It is seen that about half of the trends from the TRACE coral sets are not statistically different from zero at the 95% level. Therefore, consistent with ref. 6, it is difficult to detect a significant positive trend from a set of 50 corals of ~30 years in length. To detect with high confidence a modest linear trend in ENSO amplitude of about 15%, as in TRACE and other models[20], either more or longer corals are needed. If the coral length is maintained at 30 years but the coral members are increased to 200, the linear trend in TRACE can be detected to be significantly different from zero at the 95% level (blue curves in Extended Data Fig. 6a). If the coral members are increased to 1,000, the positive linear trend can be detected at the 99% level (black curves in Extended Data Fig. 6a).

The uncertainty in model–data comparison can also be seen in the evolution of the simulated ENSO amplitude (in the 100-year window, red in Extended Data Fig. 6b)

in comparison with the most recent reconstructions from central Pacific corals[6] and Peruvian molluscs[21], all in reference to their respective late-Holocene ENSO amplitude that is calculated as the average of the most recent millennium (1–0 kyr ago) (Extended Data Fig. 6b). Although both the model and data show an increase in ENSO amplitude from the mid to late Holocene, there are two differences between the model and data: first, the increase in ENSO is less in the model (<20%) than in data (~50%), and, second, the model does not seem to simulate a mid-Holocene minimum. If the large ENSO intensification and mid-Holocene ENSO minimum are indeed robust features for the real world, the model–data discrepancies would imply substantial model deficiencies. However, these two observational features still remain uncertain, because of the high irregularity of ENSO, the sparse data sampling and data interpretation. For example, a decrease in the window length for ENSO amplitude from 100 years to 30 years in the model (blue line in Extended Data Fig. 6b) to better represent the short length of corals would increase the spread of ENSO amplitude in the Holocene (10–0 kyr ago after detrend) 1.7-fold; the increased spread implies a greater possibility that the small number of coral records could have been influenced by the irregularity of ENSO. Using the spread of the annual range of SST along the Peru coast to infer ENSO amplitude[21] should depend on the phase-locking of ENSO with the annual cycle, and could therefore change with time if the phase-locking changes with time as in the simulation (Extended Data Fig. 10). The ensemble spread of the SST reconstructions from $\delta^{18}O$ of planktonic *Globigerinoides ruber* foraminifera in the eastern tropical Pacific[5] probably represents the total SST variability (Fig. 1f), which is dominated by the annual cycle variance, rather than ENSO variance (Extended Data Fig. 2b, c). Finally, the ENSO centre may shift between the central Pacific and eastern Pacific[21] (Extended Data Fig. 2a), which could also reshape the patterns of ENSO-related precipitation anomalies that often form the basis of palaeo-ENSO reconstructions. Ultimately, high-resolution palaeoclimate data from ENSO centres of action must be expanded significantly to resolve these issues. In particular, we suggest that various types of temperature and precipitation-sensitive proxy records from ENSO's centre of action—the central equatorial Pacific (Extended Data Fig. 2c, d)—may provide particularly effective benchmarks for model simulations of ENSO variability.

Estimating ocean–atmosphere feedback. To examine the role of ocean–atmosphere feedback in ENSO evolution, we estimate ocean–atmosphere feedbacks in the tropical Pacific in TRACE by analysing the surface ocean heat budget[23]. We first linearize the SST equation in the mixed layer as

$$\frac{\partial T}{\partial t}=Q-\frac{\partial(\bar{u}T)}{\partial x}-\frac{\partial(\bar{v}T)}{\partial y}-\frac{\partial(\bar{w}T)}{\partial x}-u\frac{\partial\bar{T}}{\partial x}-v\frac{\partial\bar{T}}{\partial y}-w\frac{\partial\bar{T}}{\partial z} \quad (1)$$

where the overbar denotes the annual mean climatology, T is SST anomaly, Q is the total surface heat flux and (u, v, w) are ocean current velocity. By integration above the mixed-layer depth (H_1) and then averaging it over a region in the eastern equatorial Pacific, denoted in angle brackets, equation (1) can be approximated as

$$\begin{aligned}\frac{\partial\langle T\rangle}{\partial t}&=\langle Q\rangle-\left(\frac{(\bar{u}T)_{\mathrm{EB}}-(\bar{u}T)_{\mathrm{WB}}}{L_x}+\frac{(\bar{v}T)_{\mathrm{NB}}-(\bar{v}T)_{\mathrm{SB}}}{L_y}\right)\\&-\left\langle\frac{\partial\bar{T}}{\partial x}\right\rangle\langle u\rangle-\left\langle\frac{\partial\bar{T}}{\partial z}\right\rangle\langle H(\bar{w})w\rangle+\left\langle\frac{\bar{w}}{H_1}\right\rangle\langle H(\bar{w})T_{\mathrm{sub}}\rangle\end{aligned} \quad (2)$$

where $H(x)$ is the Heaviside step function; $H(x)=1$ if $x\geq 0$ and $H(x)=0$ if $x<0$. Here, all the terms are derived similar to those in ref. 23, except the second term, which represents the mean advection, with the subscripts EB, WB, NB and SB denoting the average along the eastern, western, northern and southern boundaries of the region, respectively, and L_x and L_y are the longitudinal and latitudinal widths of the region, respectively. The damping coefficients associated with the negative feedback of the surface heat flux and mean advection are derived as the regression coefficients with SST as

$$\langle Q\rangle=-\alpha_{\mathrm{s}}\langle T\rangle, \quad (3)$$

$$-\left(\frac{(\bar{u}T)_{\mathrm{EB}}-(\bar{u}T)_{\mathrm{WB}}}{L_x}\right)=-\alpha_{\mathrm{MU}}\langle T\rangle,\ -\left(\frac{(\bar{v}T)_{\mathrm{NB}}-(\bar{v}T)_{\mathrm{SB}}}{L_y}\right)=-\alpha_{\mathrm{MV}}\langle T\rangle$$

The atmospheric response sensitivity to the eastern Pacific SST is estimated approximately in the regression coefficient μ_{a} between the cross-basin mean atmospheric wind (stress, $[\tau_x]$) and the eastern Pacific SST as

$$[\tau_x]=\mu_{\mathrm{a}}\langle T\rangle \quad (4)$$

The entrainment temperature is proportional to the depth of the local thermocline $\langle h\rangle$ as

$$\langle H(\bar{w})T_{\mathrm{sub}}\rangle=a_h\langle h\rangle \quad (5)$$

Finally, the oceanic response sensitivities to the wind stress are regressed as

$$\langle h\rangle-\langle h\rangle_{\mathrm{W}}=\beta_h[\tau_x],\ \langle H(\bar{w})w\rangle=-\beta_{\mathrm{W}}[\tau_x],\ \langle u\rangle=\beta_u[\tau_x] \quad (6)$$

for the thermocline slope, upwelling and zonal current, respectively. Here, $\langle h\rangle_{\mathrm{W}}$ is the thermocline depth in the western equatorial Pacific. With all the regression coefficients in equations (3–6), equation (2) can be approximated as

$$\partial\langle T\rangle/\partial t=R\langle T\rangle$$

where the total feedback parameter, or the BJ index, is

$$R=-\alpha_{\mathrm{s}}-\alpha_{\mathrm{MA}}+\mu_{\mathrm{a}}\beta_{\mathrm{u}}\langle-\bar{T}_x\rangle+\mu_{\mathrm{a}}\beta_{\mathrm{w}}\langle-\bar{T}_z\rangle+\mu_{\mathrm{a}}\beta_{\mathrm{h}}\langle\bar{w}/H_1\rangle a_{\mathrm{h}}$$

The BJ index consists of five feedbacks terms, which are, in order, the surface heat flux feedback, the mean advection feedback ($\alpha_{\mathrm{MA}}=\alpha_{\mathrm{MU}}+\alpha_{\mathrm{MV}}$), the zonal advection feedback, the local upwelling feedback, and the thermocline feedback. The last three feedbacks are all proportional to the atmospheric response sensitivity (μ_{a}), and each is further proportional to its own oceanic response sensitivities (β). Here, we choose H_1 as 50 m, w and $\bar{w}$ as the anomalous and climatological upwelling at 50 m, h approximately as the heat content anomaly, which is derived as the column-weighted temperatures at the three model levels of 4 m (surface), 56 m and 149 m, and $\bar{T}_z$ as the difference in climatological temperatures between the surface and 100 m. All the climatology variables are derived as the time-mean over a sliding window of 100 (or 300) years, and the anomalies are the monthly deviations from the climatological seasonal cycle.

For the eastern part of the equatorial Pacific (180–80° W, 5° S–5° N), which is the region of dominant ENSO variability (Extended Data Fig. 2a), the BJ index is negative, mainly as a result of the mean (meridional) advection feedback (Extended Data Fig. 7b). The negative BJ index indicates that ENSO is a stable mode maintained by stochastic forcing in CCSM3, as in most CGCMs[42]. Almost all the feedbacks tend to follow the orbital forcing in the southern subtropics (Fig. 2), with the magnitude of the feedback decreasing towards the early Holocene, but increasing towards both the late Holocene and the LGM. There is also significant millennial variability reminiscent of the meltwater forcing during the early deglaciation, especially in the upwelling feedback. The dominant role of orbital forcing for the slow evolution throughout the 21 kyr is also confirmed by the similar BJ indices in TRACE and ORB runs (Fig. 2d), and the dominant role of the upwelling feedback in TRACE (Extended Data Fig. 7b) and ORB (not shown). Finally, the mean advection feedback also shows an abrupt increase (less negative) at ~14 kyr ago due to the retreat of the ice sheet, a point that is returned to below.

The BJ index is consistent with the ENSO amplitude over most of the Holocene, both increasing from 8 kyr ago towards the late Holocene (Fig. 2b, d, or Extended Data Fig. 7a). Therefore, ENSO intensification in the Holocene can be interpreted from the linear instability perspective as being caused by increased ocean–atmosphere feedback. The increase in the BJ index is dominated by the upwelling feedback, with a minor contribution from the thermocline feedback; their sum overwhelms the decrease (more negative) in the two negative feedbacks (Extended Data Fig. 7b), leading to a modest increase in the total feedback and, in turn, the ENSO amplitude (Extended Data Fig. 7a). The increases in the three positive feedbacks are contributed by a common atmospheric response sensitivity (μ_{a}; Extended Data Fig. 8a) as well as by their respective oceanic response sensitivities (β) (Extended Data Fig. 8b, c, d).

In more detail, the upwelling feedback is further enhanced significantly by the intensified stratification (Extended Data Fig. 8f), which is caused by the precessional forcing of the subtropical South Pacific[12]. The weaker stratification in the early Holocene is caused by the precessional forcing (Extended Data Fig. 9a) on the subtropical South Pacific, where the increased insolation in austral winter warms the surface water in winter (Extended Data Fig. 9b) and then the subsurface thermocline all year round through late winter subduction (Extended Data Fig. 9c); the warmer subduction water is eventually transported into the equatorial thermocline, warming the subsurface and decreasing the stratification (Extended Data Fig. 9d). Our further calculations with various domain choices for the eastern Pacific show that the dominant contribution of the upwelling feedback is robust. The small zonal advection feedback in Extended Data Fig. 7b is caused partly by a small climatological SST zonal gradient averaged across the region—that is, $\langle-\bar{T}_x\rangle$—which is proportional to the small difference of climatological SST between the eastern and western boundaries of the eastern Pacific domain chosen here (180° W versus 80° W). With other choices of the domain, such as the Niño3.4 domain (170° W versus 120° W), the increase in the zonal advection feedback in the Holocene is larger, but still smaller than that of the upwelling feedback.

In contrast to the Holocene, during the deglacial period (~18–8 kyr ago), the BJ index does not covary with the ENSO amplitude for millennial variability, for example around the periods of HS1 and YD. The millennial modulation of ENSO therefore cannot be attributed to the change in feedbacks. The millennial modulation of ENSO varies out of phase with the seasonal cycle and therefore can be attributed to

the interaction with the seasonal cycle through the nonlinear mechanism of frequency entrainment[27], with the equatorial seasonal cycle altered by the meltwater water discharge through the AMOC[26]. The response sensitivities, the climatological states and in turn the three positive feedbacks (Extended Data Fig. 7b) all evolve in more complex patterns during the deglacial than in the Holocene. The negative feedback in heat flux shows only modest changes. The most striking change is an abrupt decrease (less negative) in the mean advection damping at ~14 kyr ago (Extended Data Fig. 7b), which is contributed mainly by the mean zonal advection. This abrupt weakening of the mean (zonal) advection damping is caused by the large retreat of ice sheet at 14 kyr ago, and is consistent with the abrupt increase of ENSO amplitude (Fig. 3a) and mean (zonal) advection feedback (similar to that in Extended Data Fig. 7b) in the ICE run at ~14 kyr ago. The abrupt intensification of ENSO at ~14 kyr ago in ICE is caused by frequency entrainment through the sudden decrease in the annual cycle (Fig. 3b). The decreased annual cycle is associated with an annual mean SST in the eastern Pacific that is more symmetrical about the Equator, which is forced by the atmospheric teleconnection response to the large retreat of the North America ice sheet at ~14 kyr ago. The retreat of the ice sheet induces a northward migration of the atmospheric westerly jet over the North Atlantic, an increase in surface easterly in the tropical North Atlantic and in turn the tropical eastern Pacific; the retreat of the ice sheet also changes the atmospheric stationary wave response, which leads to a cooling and an expansion of sea ice over the subpolar North Pacific, and also an intensified trade wind in the eastern Pacific. Either way, the intensified trade wind in the eastern Pacific propagates equatorwards through ocean–atmosphere coupling, leading to a cooling north of the Equator, which decreases the SST gradient northwards and leads to an annual mean SST that is more symmetrical about the Equator in the eastern Pacific. The detailed mechanism of the ENSO response in ICE is beyond the scope of this study and will be presented elsewhere.

31. Collins, W. *et al.* The community climate system model version 3 (CCSM3). *J. Clim.* **19,** 2122–2143 (2006).
32. Berger, A. Long-term variations of daily insolation and quaternary climatic changes. *J. Atmos. Sci.* **35,** 2362–2367 (1978).
33. Joos, F. & Spahni, R. Rates of change in natural and anthropogenic radiative forcing over the past 20,000 years. *Proc. Natl Acad. Sci. USA* **105,** 1425–1430 (2008).
34. Peltier, W. Global glacial isostasy and the surface of the ice-age earth: the ICE-5G (VM2) model and GRACE. *Annu. Rev. Earth Planet. Sci.* **32,** 111–149 (2004).
35. He, F. *Simulating Transient Climate Evolution of the Last Deglaciation with CCSM3.* PhD thesis, Univ. Wisconsin-Madison (2011).
36. McManus, J. *et al.* Collapse and rapid resumption of Atlantic meridional circulation linked to deglacial climate changes. *Nature* **428,** 834–837 (2004).
37. He, F. *et al.* Northern Hemisphere forcing of Southern Hemisphere climate during the last deglaciation. *Nature* **494,** 81–85 (2013).
38. Deser, C. *et al.* Tropical Pacific and Atlantic climate variability in CCSM3. *J. Clim.* **19,** 2451–2481 (2006).
39. Rittenour, T., Brigham-Grette, J. & Mann, M. El Niño-like climate teleconnections in New England during the late Pleistocene. *Science* **288,** 1039–1042 (2000).
40. McGregor, S. *et al.* Inferred changes in El Niño-Southern Oscillation variation over the past six centuries. *Clim. Past* **9,** 2269–2284 (2013).
41. Brown, J. *et al.* Issues in quantitative model–proxy data comparisons. *Paleoceanography* **23,** PA3202 (2008).
42. Kim, S. & Jin, F. An ENSO stability analysis. Part II: results from the twentieth and twenty-first century simulations of the CMIP3 models. *Clim. Dyn.* **36,** 1609–1627 (2010).

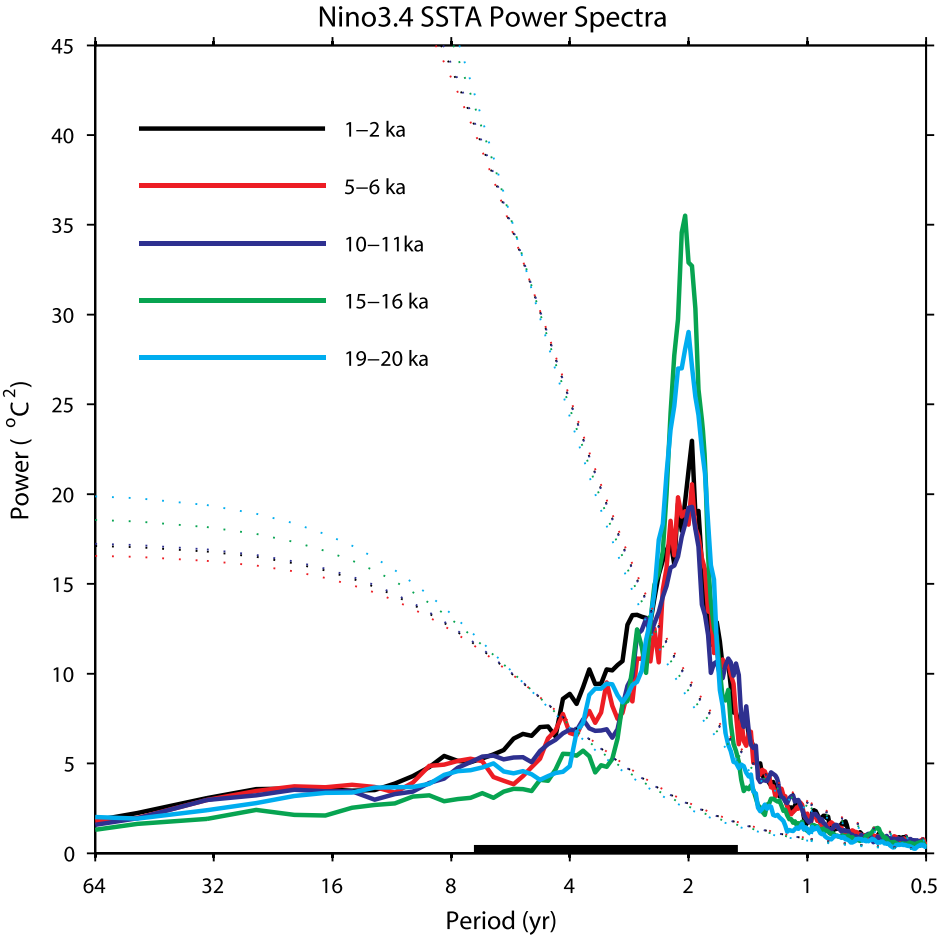

Extended Data Figure 1 | Power spectrum of ENSO. Power spectra of Niño3.4 monthly SST variability in TRACE (after removing the annual cycle) in five 1,000-year windows: 1–2 kyr ago, 5–6 kyr ago, 10–11 kyr ago, 15–16 kyr ago and 19–20 kyr ago. The spectral peak remains at ~2 years, but with a different intensity. For each spectrum, the 95% cut-off level and the corresponding red noise curve are also plotted (in dotted lines). The black bar at the bottom shows the 1.5–7-year band used for the calculation of ENSO variance.

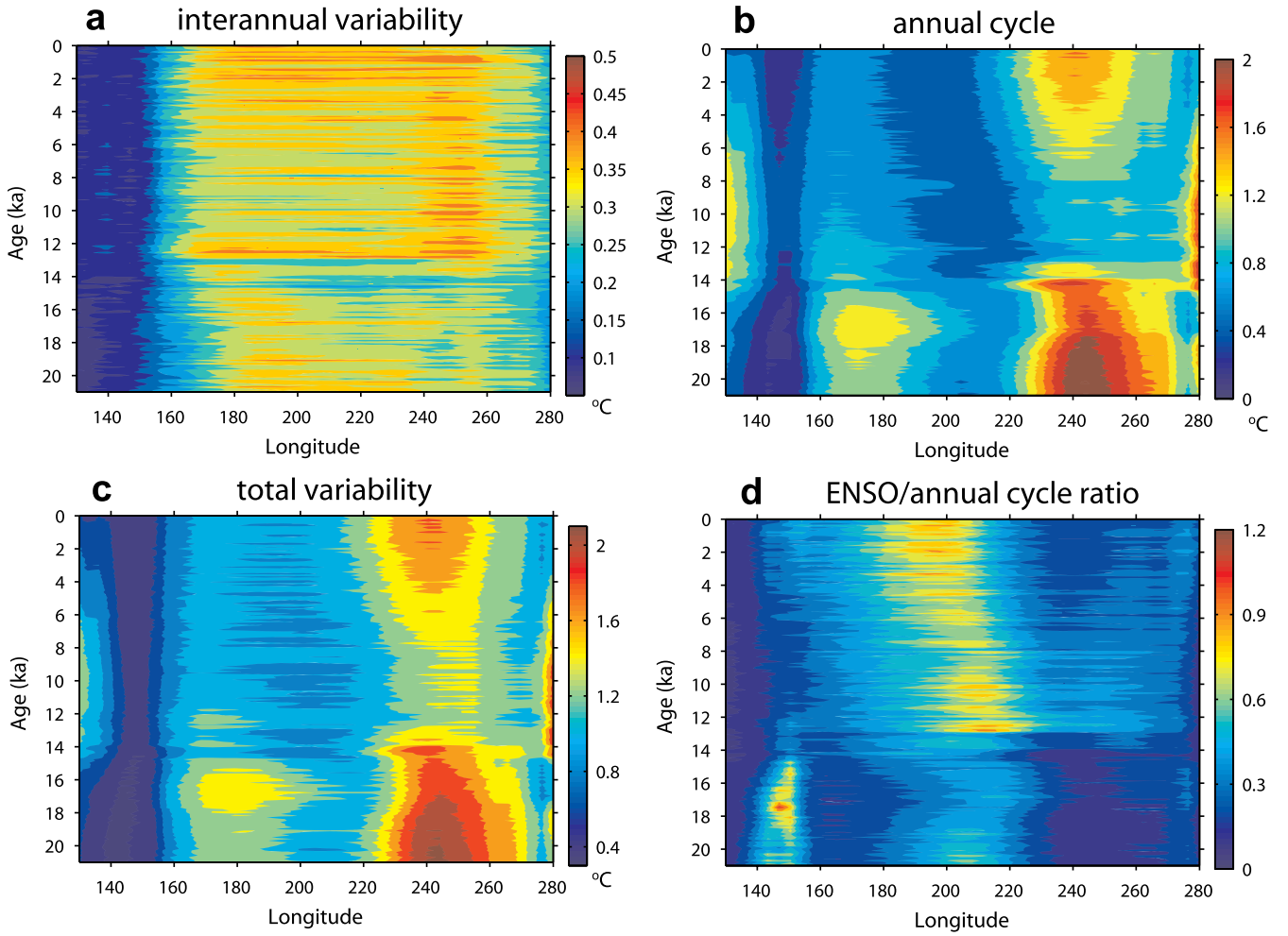

Extended Data Figure 2 | Evolution of ENSO and annual cycle along the Equator. Evolution of the amplitudes (standard deviation in 100-year window) of interannual (1.5–7 years) variability (**a**), the annual cycle of SST (**b**), total variability (<7 years) (**c**) and the ratio of the amplitudes of the interannual over the annual cycle (**d**) along the equatorial Pacific (5° S–5° N) in TRACE. The total variability is dominated by the annual cycle, except in the central-eastern Pacific, where ENSO becomes dominant. This occurs because ENSO variability shows a broad pattern from the central to the eastern Pacific, whereas the annual cycle is strong along the eastern boundary and decays rapidly towards the central Pacific.

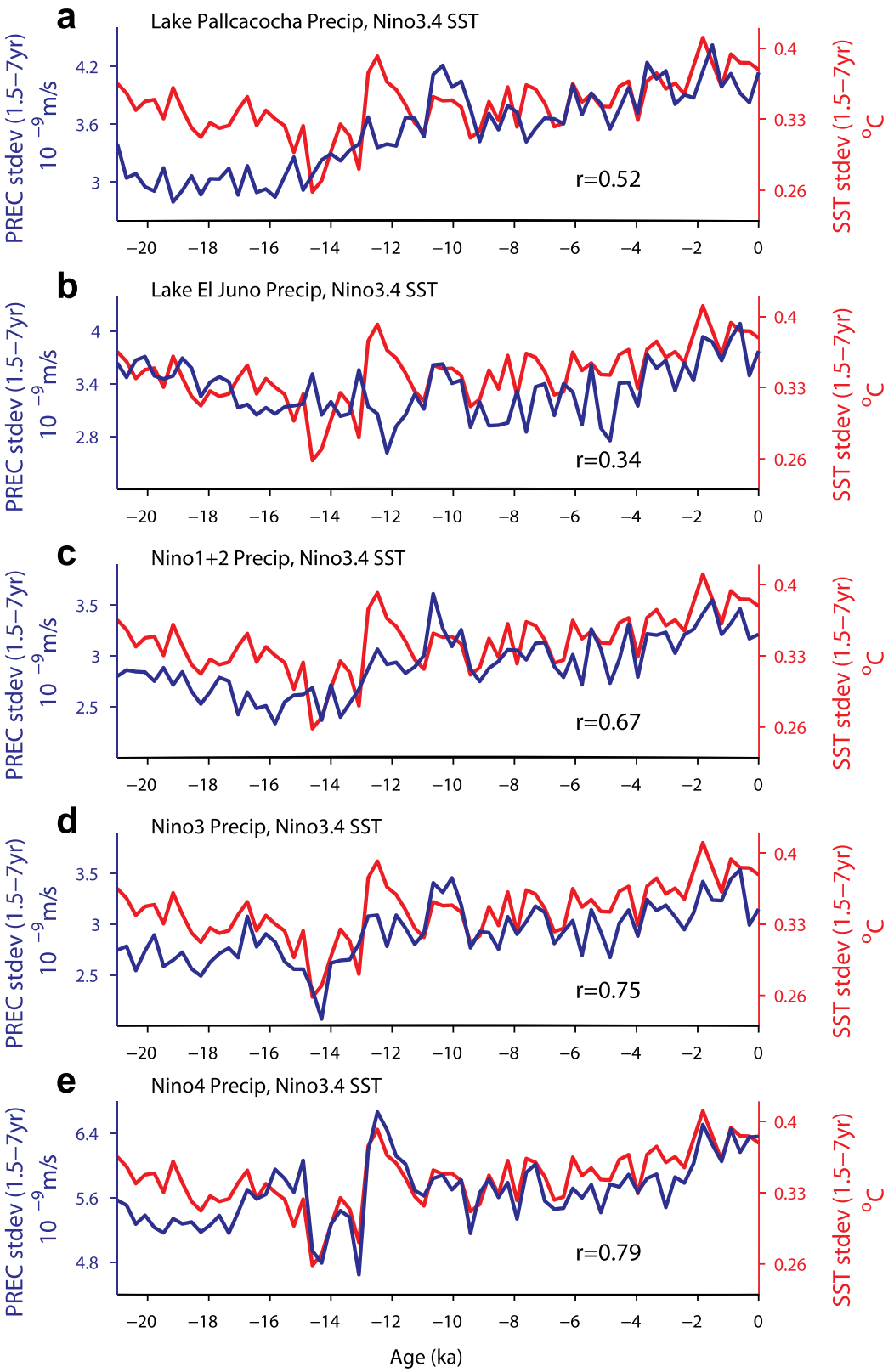

Extended Data Figure 3 | Evolution of variability amplitude. Evolution of the amplitude of interannual (1.5–7-year) variability of precipitation (blue) in TRACE in Ecuador[2] (**a**), the Galapagos islands (Lake El Juno)[7] (**b**), Niño1 + Niño2 (**c**), Niño3 (**d**) and Niño4 (**e**) (locations marked in Extended Data Figs 4 and 5). All the anomalies are the monthly data with a 3-month running mean filtered to the 1.5–7-year band. The amplitude is calculated as the standard deviation of the 1.5–7-year band-passed monthly time series in succeeding 300-year windows. For reference, the amplitude of Niño3.4 SST interannual variability is also plotted in each panel (red). The correlation between each curve and the amplitude of ENSO is also calculated. All correlations are highly significant ($P < 0.01$, with a sample size of 70).

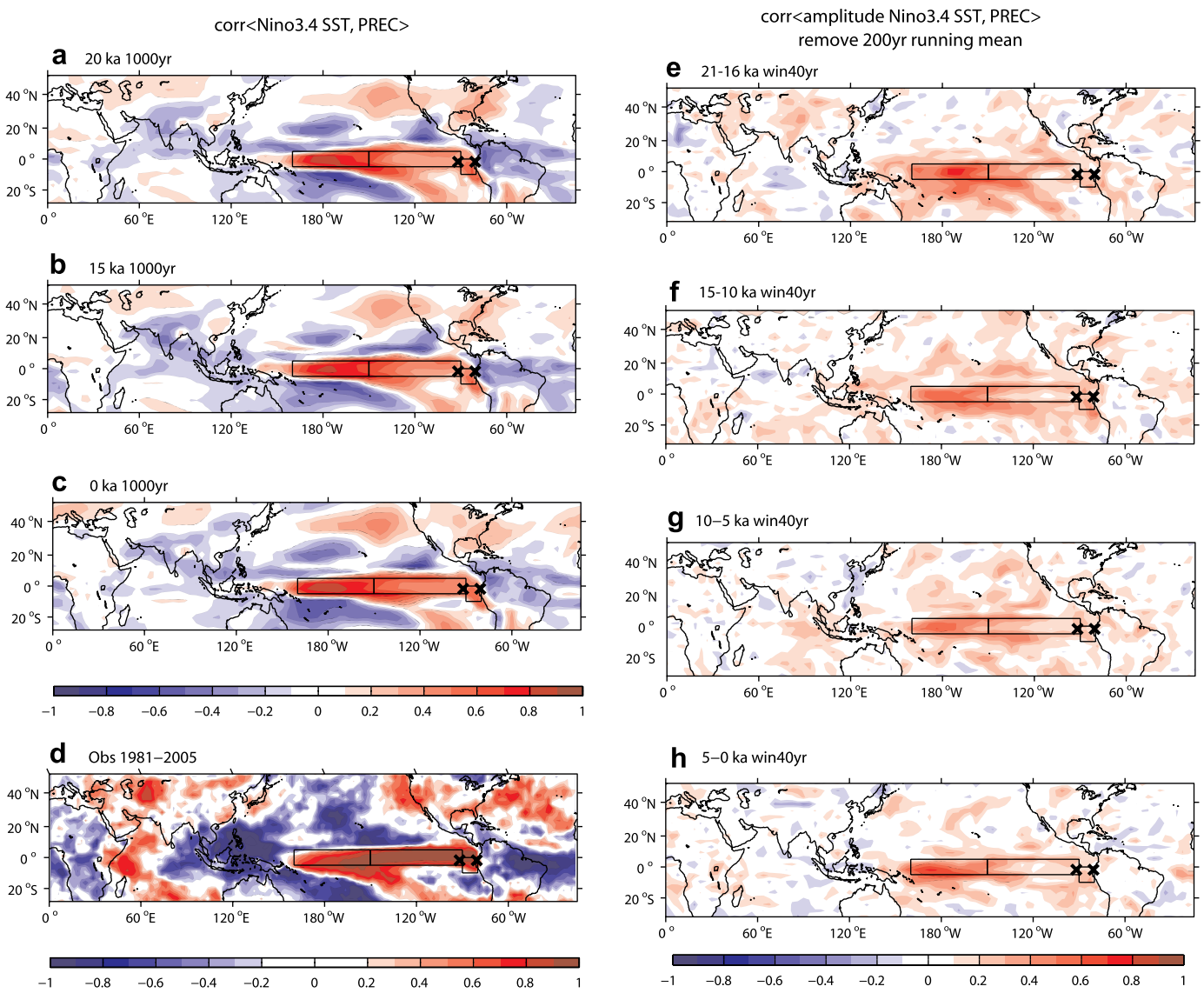

Extended Data Figure 4 | Correlation map between ENSO and precipitation. **a**–**d**, Map of time series correlation of interannual (1.5–7 yr) variability between monthly Niño3.4 SST and precipitation during 21–20 kyr ago (**a**), 16–15 kyr ago (**b**) and 1–0 kyr ago (**c**) in TRACE, and the present observation (1981–2005) (**d**). **e**–**h**, Map of interdecadal amplitude correlation between interannual ENSO (Niño3.4 SST) and precipitation variability during 21–20 kyr ago (**e**), 15–10 kyr ago (**f**), 10–5 kyr ago (**g**) and 5–0 kyr ago (**h**). All the anomalies are the monthly data with a 3-month running mean after filtered to the 1.5–7-year band. For **e**–**h** the amplitude is calculated as the standard deviation in a 40-year window, and the detrended amplitude in the 1,000-year period is used to calculate the amplitude correlation. The two black crosses indicate the region of proxy observation in the Galapagos islands[7] and on the Ecuador coast[2], respectively, and the three black boxes denote the regions of Niño1 + Niño2, Niño3 and Niño4 as discussed in Extended Data Fig. 3. Colours in correlations indicate regions where the correlation is significant at more than the 99% level.

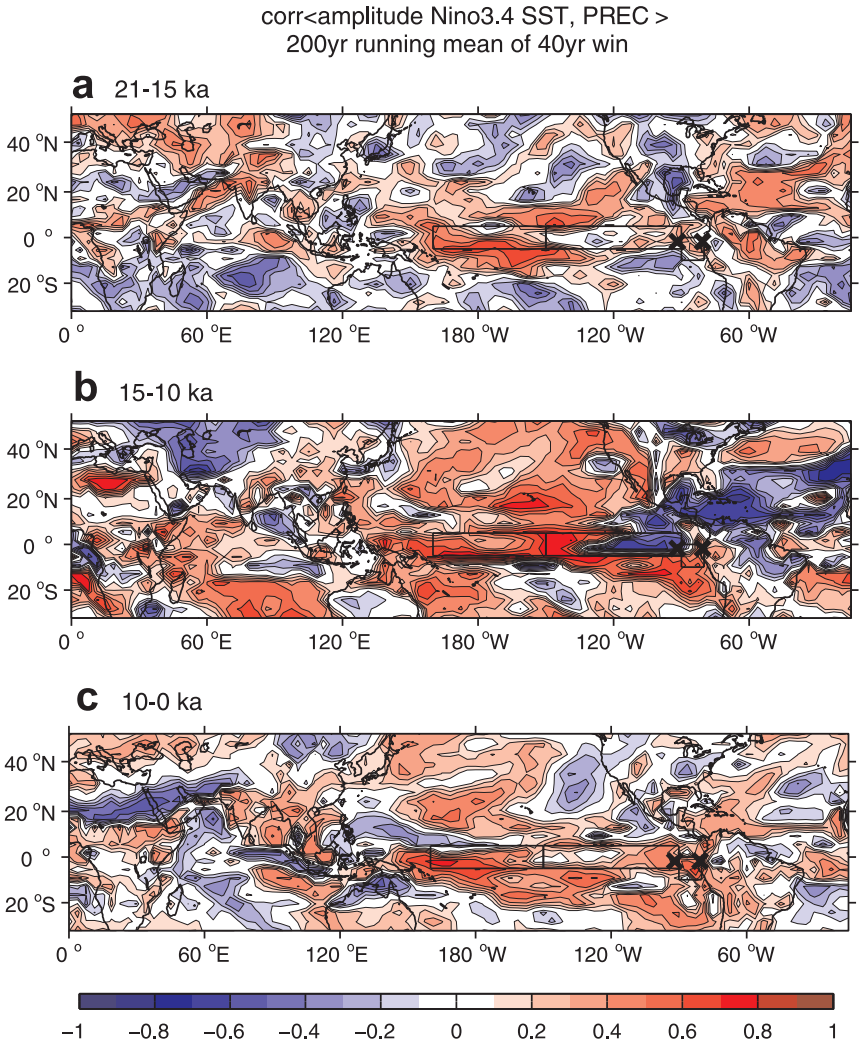

Extended Data Figure 5 | Correlation between the amplitudes of ENSO and precipitation variability. Map of the correlation between the 200-year running amplitudes of interannual ENSO and precipitation variability during 21–15 kyr ago (**a**), 15–10 kyr ago (**b**) and 10–0 kyr ago (**c**). The two black crosses indicate the region of proxy observation in the Galapagos islands[7] and on the Ecuador coast[2], respectively, and the three black boxes denote the regions of Niño1 + Niño2, Niño3 and Niño4 as discussed in Extended Data Fig. 3. The result will be similar if the amplitude is calculated directly using a 300-year window as in Extended Data Fig. 3. Colours in model correlations indicate regions where the correlations are significant at more than the 99% level.

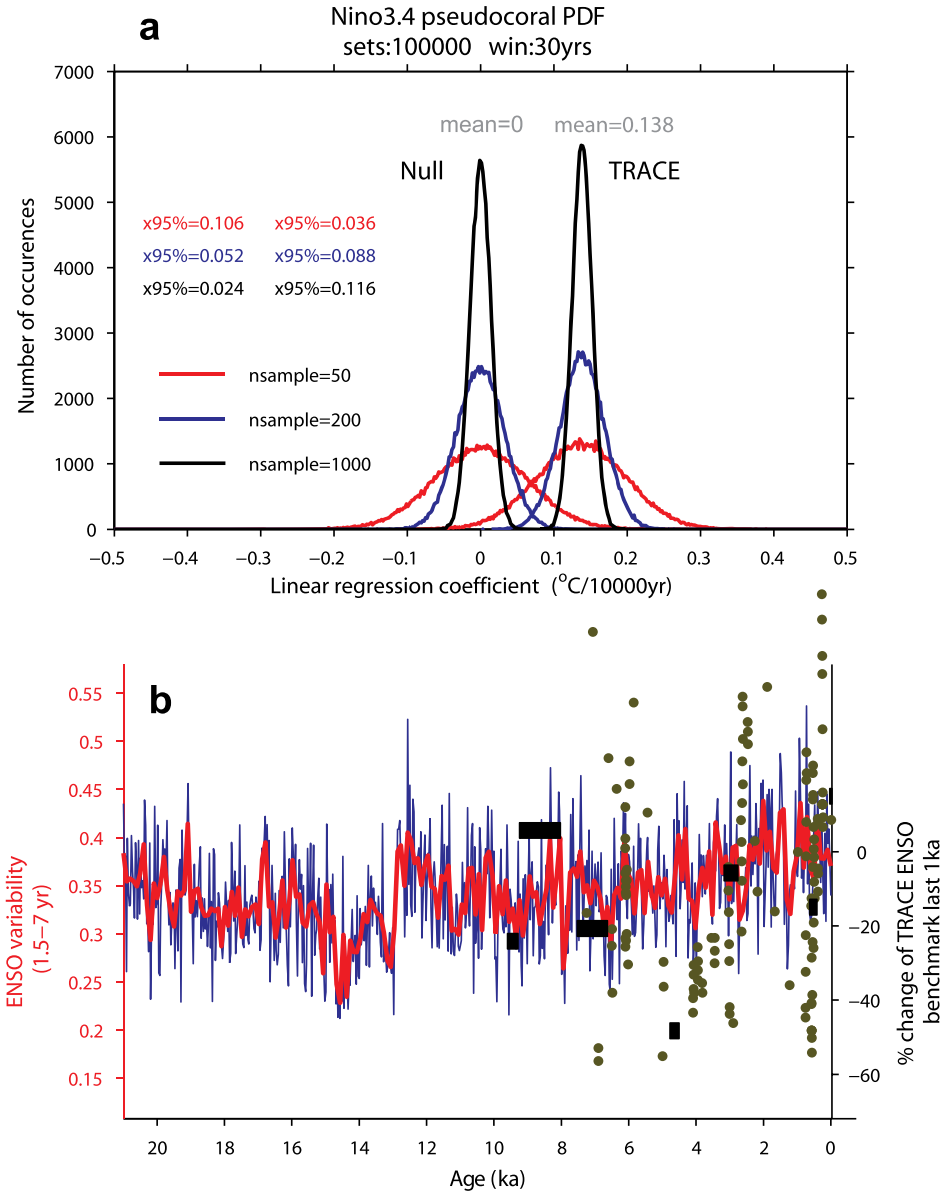

Extended Data Figure 6 | Uncertainty for ENSO model–data comparison. **a**, Detecting trend of ENSO amplitude in 'pseudo-corals'. Histogram of Holocene (7–0 kyr ago) linear trends of ENSO amplitude derived from 30-year 'pseudo-coral' records of the Niño3.4 SST in TRACE. A linear trend (regression coefficient) is derived from the ENSO amplitudes of a random set of 50 (red) 'corals', with each ENSO amplitude as the standard deviation of the interannual (1.5–7 years) SST variability of a 30-year section of 'coral record'. The PDF on the right (marked with TRACE) is derived from the linear trends of 100,000 randomly formed sets of coral records, whereas the PDF on the left (marked with Null) is the null hypothesis of no trend in ENSO amplitude, and is derived from the linear trend of a time series after random scrambling of the Niño3.4 SST. Two additional PDFs are derived with the number of corals increased to 200 (blue) and 1,000 (black) in each set. The right-side one-tailed 95% significance levels are 0.106 (red), 0.052 (blue) and 0.024 (black) for the null hypothesis, and the left-side one-tailed 95% significance levels are 0.036 (red), 0.088 (blue) and 0.116 (black) for TRACE. With 50 corals, the trend in TRACE cannot be identified at the 95% level because the significance level in TRACE is below that of NULL ($0.036 < 0.106$); with 200 corals, the trend can be identified at the 95% level because the significance level of TRACE is beyond that of NULL ($0.088 > 0.052$); with 1,000 corals, the 95% significance levels are well beyond the NULL ($0.116 \gg 0.024$), implying a highly significant trend of ENSO strengthening in the Holocene. **b**, ENSO amplitude in TRACE in a 100-year window (red thick line, same as in Fig. 1e) and a 30-year window (blue thin line) (both on the left axis) as well as the ENSO variance reconstructed from corals in the central Pacific[6] (dark green dots) and from the variance of annual SST range from mollusc shells along the Peru coast[21] (black horizontal bars). The two data sets are plotted in changes relative to the present ENSO amplitude (on the right axis), which is then rescaled with the model ENSO amplitude such that the relative change in model ENSO amplitude can also be scaled on the right axis. All the model and proxy data are aligned and referenced to their last millennium average (1–0 kyr ago).

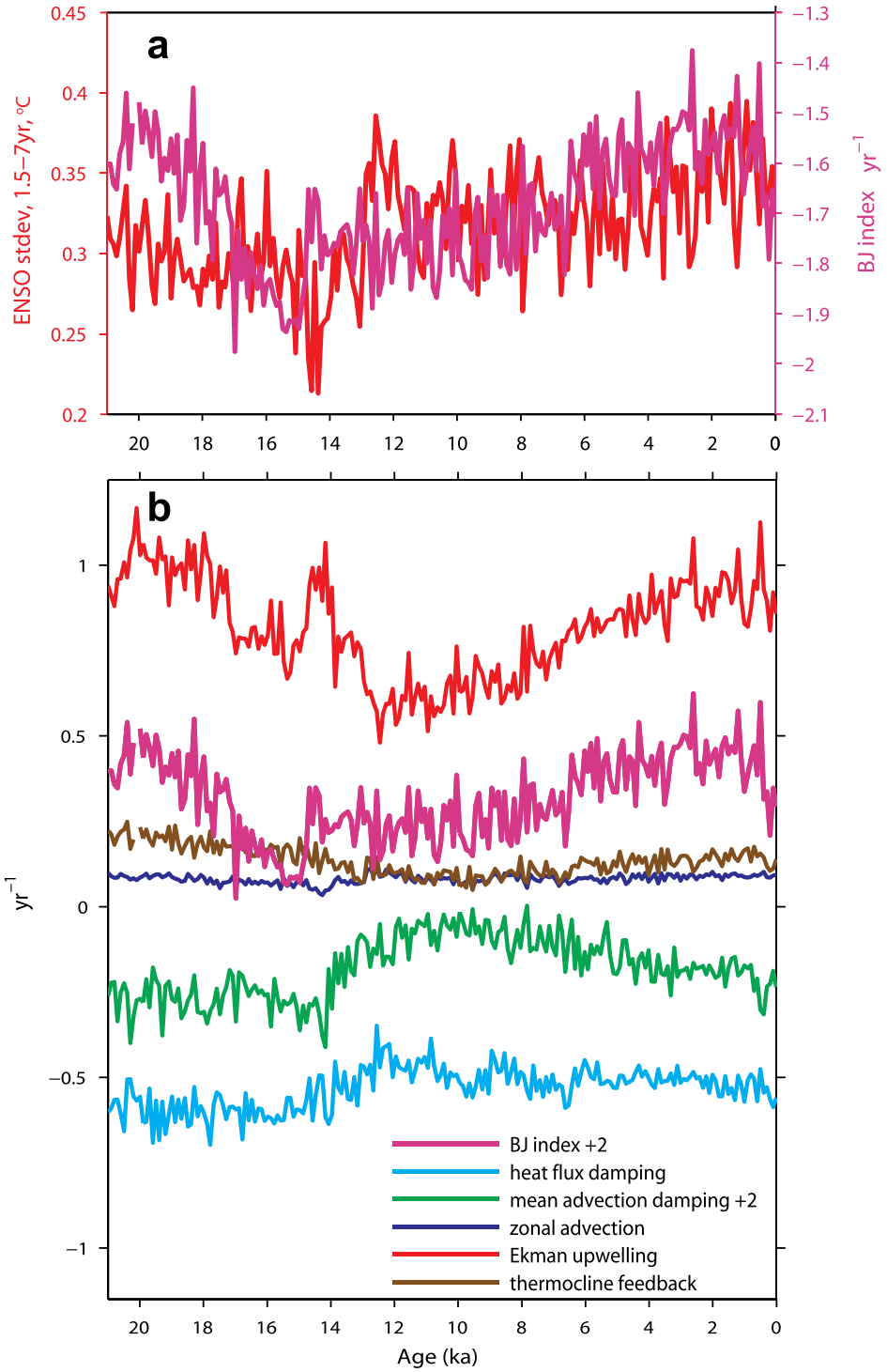

Extended Data Figure 7 | Evolution of the BJ index and its components. Evolution of ocean–atmosphere feedbacks in the eastern equatorial Pacific region (180° E–80° W, 5° S–5° N) for interannual (1.5–7-year band) ENSO variability in 100-year windows in TRACE. **a**, ENSO amplitude (red) and the BJ index (purple). **b**, The two negative (damping) feedbacks (surface heat flux feedback (cyan) and mean advection feedback (green, offset by +2)) and the three positive feedbacks (zonal advection feedback (blue), Ekman upwelling feedback (red) and thermocline feedback (brown)), as well as the (sum) total feedback (BJ index, purple, offset by +2). The ENSO amplitude largely follows the BJ index (an increasing trend) in the Holocene, but not in the deglaciation, suggesting the dominant role of ocean–atmosphere feedback for ENSO intensification in the Holocene, but not for millennial variability in deglaciation.

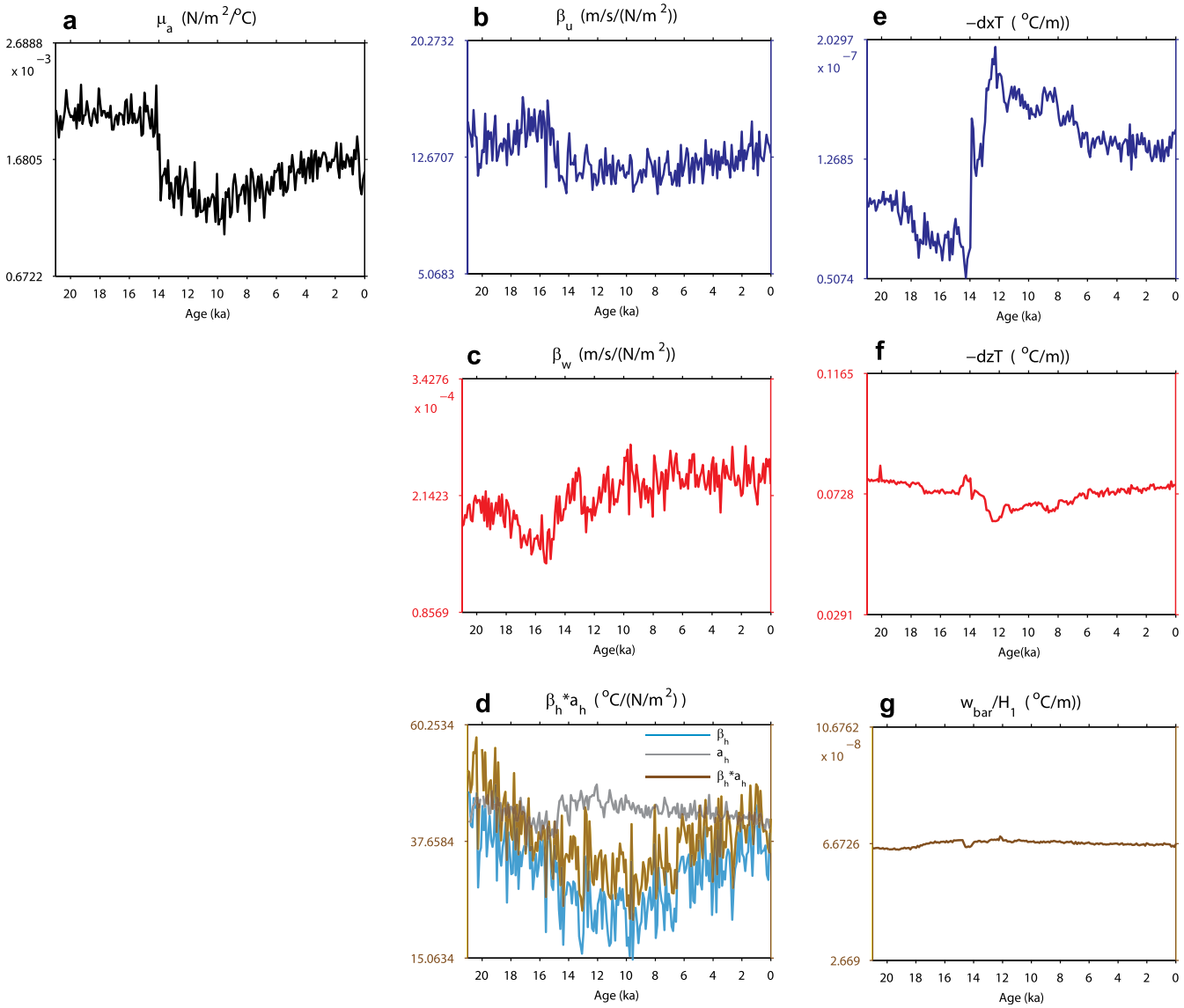

Extended Data Figure 8 | Evolution of feedback coefficients. Response sensitivity and mean state for interannual variability in the eastern equatorial Pacific region (170° E–80° W, 5° S–5° N) in TRACE. **a**, Atmospheric response sensitivity to SST. **b**, Zonal current response sensitivity to wind stress. **c**, Upwelling response sensitivity to wind stress. **d**, Thermocline response sensitivity to wind stress ($\beta_h a_h$, brown), β_h (cyan) and a_h (grey). **e**, Mean zonal SST gradient. **f**, Mean stratification. **g**, Mean upwelling. In **a**–**g**, each curve is plotted to the same relative scale such that their variation can be compared directly: the scale of a variable y ranges from median $(y) - 0.6 \times |\text{mean}(y)|$ to median $(y) + 0.6 \times |\text{mean}(y)|$.

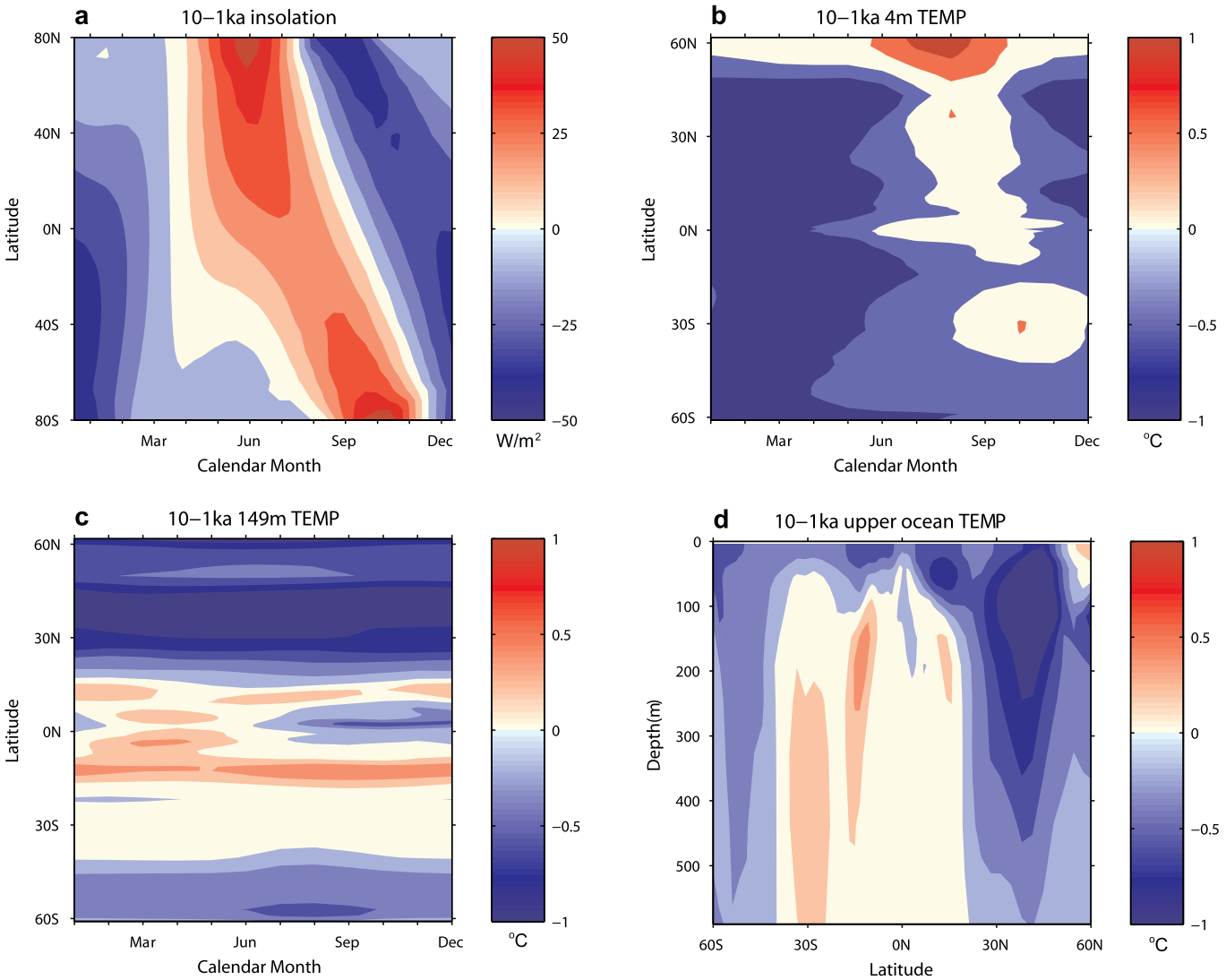

Extended Data Figure 9 | Response of equatorial thermocline in the Holocene. **a**–**c**, The annual cycle of the difference between 10 kyr ago and 1 kyr ago of insolation (**a**), and in South Pacific temperature (°C) at the surface (**b**) and 149 m depth (**c**) for different latitudes in TRACE. Zonal mean annual mean temperature difference in the upper ocean of the South Pacific (180–100° W) (**d**). In the subtropical South Pacific (40–10° S), the insolation warming in austral winter (in **a**) leads to a SST warming in austral winter–spring (in **b**), which is then ventilated into the subsurface thermocline as a warming throughout the year (in **c**), and eventually into the equatorial thermocline (in **d**), decreasing the stratification there.

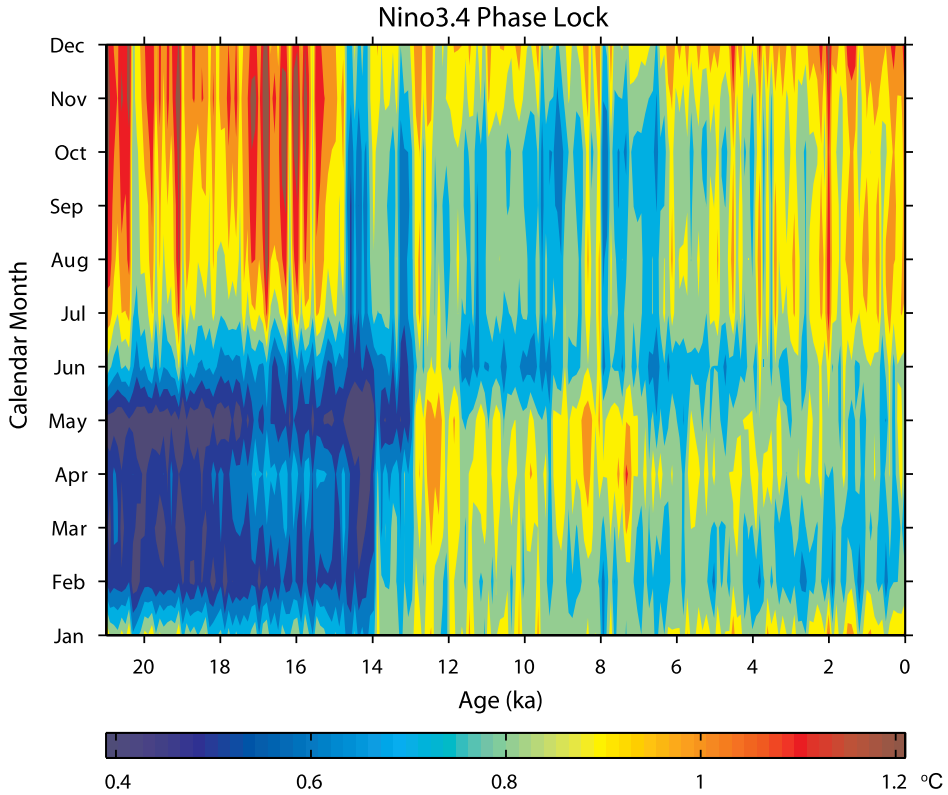

Extended Data Figure 10 | Phase-locking of ENSO. Evolution of phase locking of Niño3.4 SST interannual variability as a function of the calendar month in 100-year windows. The peak of ENSO anomaly is locked strongly to boreal winter in early deglaciation; this phase locking is weakened towards the early Holocene, but re-emerges towards the late Holocene.